BNL-114834-2017-JAAM

Synthesis, Characterization, and Growth Mechanism of Motifs of Ultrathin Cobalt-substituted NaFeSi2O6 Nanowires

C. S. Lewis, S. S. Wong

To be published in "CrystEngComm"

December 2017

Condensed Matter Physics and Materials Science Department

Brookhaven National Laboratory

U.S. Department of Energy

USDOE Office of Science (SC),

USDOE Office of Science (SC), Basic Energy Sciences (BES) (SC-22)

Notice: This manuscript has been authored by employees of Brookhaven Science Associates, LLC under Contract No. DE-SC0012704 with the U.S. Department of Energy. The publisher by accepting the manuscript for publication acknowledges that the United States Government retains a non-exclusive, paid-up, irrevocable, world-wide license to publish or reproduce the published form of this manuscript, or allow others to do so, for United States Government purposes.

DISCLAIMER

This report was prepared as an account of work sponsored by an agency of the United States Government. Neither the United States Government nor any agency thereof, nor any of their employees, nor any of their contractors, subcontractors, or their employees, makes any warranty, express or implied, or assumes any legal liability or responsibility for the accuracy, completeness, or any third party's use or the results of such use of any information, apparatus, product, or process disclosed, or represents that its use would not infringe privately owned rights. Reference herein to any specific commercial product, process, or service by trade name, trademark, manufacturer, or otherwise, does not necessarily constitute or imply its endorsement, recommendation, or favoring by the United States Government or any agency thereof or its contractors or subcontractors. The views and opinions of authors expressed herein do not necessarily state or reflect those of the United States Government or any agency thereof.

BNL-114834-2017-JA

Synthesis, Characterization, and Growth Mechanism of Motifs of Ultrathin Cobalt-substituted NaFeSi2O6 Nanowires

C. S. Lewis, S. S. Wong

Submitted to CrystEngComm

December 2017

Condensed Matter Physics and Materials Science Department

Brookhaven National Laboratory

U.S. Department of Energy
USDOE Office of Science (SC),
Basic Energy Sciences (BES) (SC-22)

Notice: This manuscript has been authored by employees of Brookhaven Science Associates, LLC under Contract No. DE- SC0012704 with the U.S. Department of Energy. The publisher by accepting the manuscript for publication acknowledges that the United States Government retains a non-exclusive, paid-up, irrevocable, world-wide license to publish or reproduce the published form of this manuscript, or allow others to do so, for United States Government purposes.

DISCLAIMER

This report was prepared as an account of work sponsored by an agency of the United States Government. Neither the United States Government nor any agency thereof, nor any of their employees, nor any of their contractors, subcontractors, or their employees, makes any warranty, express or implied, or assumes any legal liability or responsibility for the accuracy, completeness, or any third party's use or the results of such use of any information, apparatus, product, or process disclosed, or represents that its use would not infringe privately owned rights. Reference herein to any specific commercial product, process, or service by trade name, trademark, manufacturer, or otherwise, does not necessarily constitute or imply its endorsement, recommendation, or favoring by the United States Government or any agency thereof or its contractors or subcontractors. The views and opinions of authors expressed herein do not necessarily state or reflect those of the United States Government or any agency thereof.

Synthesis, Characterization, and Growth Mechanism of Motifs of Ultrathin Cobalt-substituted $NaFeSi_2O_6$ Nanowires

Crystal S. Lewis[1], Dominic Moronta[1], Maxwell W. Terban[2], Lei Wang[1], Shiyu Yue[1], Cheng Zhang[3], Qiang Li[3], Adam Corrao[1], Simon J. L.Billinge[2,3], and Stanislaus S. Wong[1,*]

[1]Department of Chemistry, State University of New York at Stony Brook, Stony Brook, NY 11794-3400

[2]Department of Applied Physics and Applied Mathematics, Columbia University, New York, NY 10027

[3]Condensed Matter of Physics and Materials Sciences Division, Brookhaven National Laboratory, Upton, NY 11973

*To whom correspondence should be addressed.

Email: Stanislaus.wong@stonybrook.edu; sswong@bnl.gov

Phone: 631-632-1703; 631-344-3178

Abstract. In this report, we have synthesized and structurally characterized nanowire bundles of cobalt-substituted pyroxenes, similar to the crystal structure of Aegirine (i.e. Co-substituted $XYSi_2O_6$ with X and Y referring to metallic elements such as but not limited to Co, Na, and Fe), using a readily scalable hydrothermal technique. We propose a growth mechanism for these bundles, based on detailed time and temperature dependent studies as well as complementary control experiments, particularly reactions in the absence of either APTES or NaOH, via a transmission electron microscopy visualization study. Moreover, these nanowire bundles were probed for their magnetic properties and chemical composition using Superconducting Quantum Interference Device (SQUID) measurements, X-ray diffraction, and pair distribution function analysis, respectively. Specifically, SQUID measurement observations highlighted that these bundles evince (i) unique and interesting super-paramagnetic properties at 5 K that are consistent with that of our previously published ~2 nm ultra-small nanoparticles as well as (ii) paramagnetic behavior at 300 K.

Keywords: $NaFeSi_2O_6$ nanowires, metal silicates, silicate nanowires, pyroxenes, magnetic nanowires

1. Introduction

Nanomaterials denote structures with at least one feature size in the range between 1 and 100 nm. As such, these structures have attracted significant research interest, due to their unique size-dependent optical, magnetic, electronic, thermal, and chemical properties as compared with those of the corresponding bulk. Specifically, one-dimensional (1D) nanomaterials, including but not limited to nanowires (NWs), nano-whiskers, and nanorods, have generated widespread attention, as they give rise to distinctive chemical and physical properties by comparison with their bulk counterparts.

In particular, 1D nanomaterials are desirable, because of their thermodynamic stability, physiochemical properties, and magnetic properties (i.e. hysteresis and Curie temperature) that are inherently dependent upon the nanowires' length, diameter, inter-wire distances (i.e. lengths less than 60 nm between the individual wires themselves, wherein magnetic dipole coupling becomes significant), and chemical composition.[1-4] Hence, due to these properties, magnetic 1D materials have been extensively probed for their potential use as viable components of spintronic devices, data storage media, and MRI contrast agents.[5, 6] For example, ferromagnetic NWs have recently been fabricated as building blocks for nanoscale magnetic logic junctions.[7, 8] Hence, the flexibility and versatility of magnetic nanostructures are potentially of significant interest for various types of applications.

A number of groups including ours have successfully synthesized a variety of magnetic materials such as various morphological manifestations of bismuth ferrite ($Bi_2Fe_4O_9$ and $BiFeO_3$), magnetite (Fe_3O_4), yttrium manganese oxide ($YMnO_3$), as well as a class of spinel ferrite (MFe_2O_4) nanoparticles using a toolkit of diverse strategies,

encompassing sol-gel template, solution evaporation, citrate combustion, molten salt, solid state, and hydrothermal syntheses.[9-18] Of these magnetic materials, MFe_2O_4 (wherein 'M' = Co, Fe, Ni, or Zn) nanostructures show particularly interesting properties in that they display superparamagnetic behavior coupled with high stability.[5, 19, 20]

As per our prior work in this area on related MFe_2O_4 systems, the effects of composition and size upon their resulting magnetic properties were probed.[14] Specifically, we had found that as the size was decreased to the ultra-small (~3 nm in diameter) size regime, these nanoparticles no longer definitively maintained a spinel structure but rather appeared to be amorphous in nature.[14] Moreover, as the overall size was decreased to these ultra-small spherical particles, superparamagnetic behavior was observed. Hence as an extension of our previous studies, the focus of the current work herein has been to confirm the overall structure of our as-prepared, anisotropic ultrathin (i.e. ~2 nm in diameter) NWs with the overall objective of correlating their magnetic properties with their corresponding structure.

The coating of metal oxides with an insulating layer, such as a silica coating, has become a vitally important strategy for solubilizing these materials (especially at the nanoscale) for various practical applications such as but not limited to catalysis, sensing, and biomedicine.[21-27] In practice, the coupling with alkoxysilanes, such as 3-aminopropyltriethoxy silane (APTES) as an illustrative example, has become one of the more popular experimental strategies for modifying the surfaces of nanoparticles, such as magnetic nanostructures, for imaging and drug delivery, for instance.[28-33] More specifically, these alkoxysilanes tend to induce the formation of silicate chains, surrounding the surfaces of the nanoparticles.[14, 34] An example of a possible motif

resulting from such interactions is the formation of pyroxene structures characterized by the generalized formula of $XY(Si,Al)_2O_6$, wherein 'X' represents either Na^{2+} or Fe^{2+} and 'Y' stands for Fe^{3+}. From a geological perspective, interactions of metals with silicate chains, as is prevalent within pyroxene-type structures, are characteristic of volcanic types of materials, which are a component of the Earth's mantle (~20%), thereby rendering metal silicates as a relatively earth-abundant species.[35-37]

In this study, we have likely created the cobalt-substituted pyroxene-type silicates with a generic composition of $XYSi_2O_6$ (wherein both 'X'= mono- or divalent metals and 'Y'= divalent or trivalent metals).[38] In general, pyroxenes possess a crystal structure associated with either an orthorhombic or a monoclinic symmetry. Herein, we find that the local structure of our NWs most closely resembles that of Aegirine, characterized by not only a chemical composition of $NaFeSi_2O_6$ but also a monoclinic unit cell with a space group C12/c, incorporating single chains of SiO_4 tetrahedra.[38] The crystalline environment of these materials, particularly with respect to the orientation of the chains of these constituent SiO_4 tetrahedra, was thought to induce a 'geometric magnetic frustration' effect,[39, 40] implying the controversial possibility of structure-mediated ferromagnetic or antiferromagnetic behavior, depending upon the precise chemical composition.[41-43] However, according to the prior studies of Aronson et al., antiferromagnetic behavior is likely to be primarily caused by weak interactions between the transition metal ion sites themselves as opposed to structural considerations.[39]

Synthetic pyroxenes have been successfully generated through protocols wherein the composition, size, and morphology of these materials were precisely controlled through judicious variations of reaction time, temperature, and surfactant.[44-46] It is worth

specifically noting that a few types of pyroxenes have been readily synthesized in the guise of various unique motifs, such as three-dimensional (3D) hollow nanospheres and two-dimensional (2D) nanoflakes, via hydrothermal and calcination processes, respectively.[45, 47-49] The implication therefore is that reaction parameters can be used to finely tune the morphology and hence, the magnetic properties of these materials. In addition to being good insulators, metal silicate materials are also transparent crystals, thereby denoting their possible relevance for possible opto-electronic applications.[40, 50] In particular, studies have shown that the use of nanoscale aegirine ($NaFeSi_2O_6$) yielded efficient absorptive removal of violanthrone-79, a model heavy hydrocarbon compound; as such, these materials are highly sought after by the petrochemical industry for catalytic absorption processes, important for oil remediation.[44]

From a synthetic point of view, we emphasize that all of our ultra-small motifs (i.e. nanowires and particles) were prepared in the presence of APTES, a molecule not typically used to control size. Hence, from a chemical functionality perspective, we consider that APTES behaves as a surfactant. It is well known that the presence of surfactants can potentially alter the particle sizes of nanostructures by creating a barrier for mass transfer, thereby modulating the surface energy of growing facets as well as inhibiting nanoparticle agglomeration. We note that our previous work[14] had briefly highlighted interactions between metal ions in solution with APTES under basic environments as the primary reason for the fabrication of the resulting ultra-small (i.e. ~3 nm in average diameter) particles. Hence, in an effort to further probe the synergistic effects that both surfactant and the presence of base yield with respect to nanostructured

growth, a systematic study has been employed to confirm if indeed both reaction variables aid in the production of the overall resulting morphology.

As a result, our contribution has been to use a generalized method for reproducibly synthesizing crystalline cobalt-substituted pyroxene-type NWs of definable morphology and motif, while exhibiting chemical control over the metal ions within the pyroxene crystal structure. Though $NaFeSi_2O_6$ nanowire (NW) bundles have been synthesized previously using the hydrothermal method,[45] we have pursued the idea herein of rationally modifying ultrathin constituent variants of this material by atomic chemical substitution with a transition metal species. In so doing, our objective has been to correlate both morphology and chemical composition with the resulting magnetic properties of these NWs by using SQUID magnetometry.

Furthermore, we are the first to propose a growth mechanism for the formation of these nanowire bundles by systematically varying the time, temperature, and surfactant used in the hydrothermal reaction in an effort to more precisely understand the role of each parameter in determining the resulting 1D anisotropic growth of these metal-substituted pyroxenes. Through these systematic variations, it is clear that the presence of base (i.e. NaOH) as well as that of the silica source / templating agent (i.e. APTES) play an inherent and important role in the growth of the observed nanowire bundles.

2. Experimental

2.1. Materials and Reagents. To generate these Co-substituted $NaFeSi_2O_6$ NW bundles, the following chemicals were used. Specifically, cobalt chloride hexahydrate, (98%, Aldrich), iron (III) chloride hydrate (99.8%, Mallinckrodt), sodium hydroxide (99%,

EMD Science), potassium hydroxide (86.9%, Fischer), ammonium hydroxide (28-30% NH_3 in water, Acros Organics) aminotriethoxysilane (APTES, 99% Acros Organics), tetraethyl orthosilicate (TEOS, 98%, Aldrich), and tetramethyl orthosilicate (TMOS, 98%, Aldrich) were all utilized.

2.2. Methodology.

Co-substituted $NaFeSi_2O_6$ NW bundles were prepared using a modified protocol for the hydrothermal method, as previously reported by our lab.[14] Briefly, 0.02 M of $CoCl_2$ was dissolved in 15 mL of distilled water in a beaker and then stirred at ~300 rpm for 15 minutes. Subsequently, 0.04 M of $FeCl_3$ was also added to the beaker and dissolved in solution under continuous stirring. It is important to note that the molarities of the metal precursor solutions were calculated using the volume of the final solution, namely 18.3 mL, in order to fill ~80% of the volume of a 23 mL Teflon-lined container that was subsequently transferred to a steel autoclave. Finally, 2.3 mL of 4.4 M NaOH, used as means of controlling pH as well as of solubilizing the metal cationic complexes, coupled with 1 mL of APTES, functioning as the surfactant / silica source, were injected into the mixture, and vigorously stirred for 30 minutes.

As per our prior experience with ferrite-based systems, the role of the NaOH is to modulate pH and the solubility of the metal precursors, thereby inducing the formation of soluble metal derivatives (i.e. metal hydroxides), a finding consistent with not only Massart's prior work on synthesizing Fe_3O_4 in an alkaline medium but also the intrinsic Pourbaix diagram itself of iron which predicts the formation and stability of metal hydroxides under these favorable basic conditions.[51, 52] Subsequently, these soluble metal derivatives stabilize the linear silicate chains of APTES through electrostatic

interactions.[14] Additionally, we noted that in the presence of APTES, our so-called 'surfactant' / templating agent, we could achieve control over the size and physical features of NW bundles of Co-substituted $NaFeSi_2O_6$. Hence, we emphasize that the presence of both additives is important, leading to selective adsorption of metal ions coupled with favorable and cooperative interactions among the APTES, the metal ions, as well as the Na^+ ions. These likely collectively and synergistically impact upon the resulting nucleation process and hence, the subsequent observed morphology.

Upon addition of NaOH, there was a perceptible color change from an orange to a dark brown hue, thereby signifying the precipitation of the metal-based precursors. After stirring for 30 minutes, the solution was transferred to a 23 mL Teflon-lined steel autoclave (Parr Instruments) and sealed. The autoclave was then placed in an oven and heated at 220°C for 3 to 10 hours. After heat treatment, the product was collected (~150 mg), and it was washed three times with distilled water and once more with an aliquot of ethanol, prior to final oven drying of the product at ~80°C in order to remove any residual solvents. After oven drying, the samples were ground for an additional 30 minutes using a mortar and pestle for further structural characterization.

Initial control experiments, wherein (i) NaOH was substituted with other bases, such as potassium hydroxide (KOH) and ammonium hydroxide (NH_4OH), sought to probe the significance of the cationic identity (i.e. Na^+ versus K^+ versus NH^{4+}) of the base itself with respect to modulating nanowire growth. Specifically, this paper aims to determine whether replacing NaOH with hydroxide ion analogues could lead to the formation of products, possessing similar composition and morphological features. In the specific case of NH_4OH, i.e. a weaker base, we were interested in deducing a potential

connection and correlation between the strength of the base, the size of the counter-ion, and the synthesis of the resulting metal oxide species. We describe all of these control experiments along with the associated findings in the Supporting Information section. Furthermore, a number of additional control experiments wherein (ii) APTES was replaced with different silicate derivatives, such as tetraethyl orthosilicate (TEOS) and tetramethyl orthosilicate (TMOS), were run in an analogous manner. Systematic variations in reaction time, temperature, and surfactant were also explored.

2.3. *Characterization.*

2.3.1. **Pair Distribution Function (PDF) Measurement & Analysis**

X-ray total scattering measurements were carried out at the XPD beamline (X-ray Powder Diffraction, 28-ID-2), which is part of the National Synchrotron Light Source (NSLS)-II synchrotron light source, located at Brookhaven National Laboratory. NW bundles, sealed in 1 mm ID kapton capillary tubes, were measured with the rapid acquisition PDF mode[53] with an X-ray energy of 67.795 keV (0.18288 Å) using a Perkin-Elmer 2D detector (2048 x 2048 pixels and 200 x 200 μm pixel size) mounted orthogonal to the incident beam path with a sample-to-detector distance of 204.2825 mm. Calibration of the detector geometry was carried out using a standard Ni sample mounted in the sample holder. The raw 2D data were azimuthally integrated and converted to plots of 1D intensity versus the magnitude of the momentum transfer, Q (wherein $Q = 4\pi\sin\theta/\lambda$ for elastic scattering), using the program FIT2D.[54]

The PDF gives the scaled probability of finding a pair of atoms separated by a distance of r. Background subtraction and data reduction of the 1D scattering data were performed using the program PDFgetX3[55] in xPDFsuite.[56] Experimental PDFs, G(r),

were obtained through Fourier transformation, according to Equation 1, by

$$G(r) = \frac{2}{\pi}\int_{Q_{min}}^{Q_{max}} Q[S(Q)\text{-}1] \sin Qr \, dQ, \qquad \text{(Eq. 1)}$$

wherein *S(Q)* is the total scattering structure function measured from Q_{min} to Q_{max}. In this case, the range of Q spans from 0.77 to 22.0 Å^{-1}.[57] Model fitting to the PDF data was performed using the program PDFgui.[58] Structure models were fit by refining the lattice parameters and atomic positions allowed by symmetry, isotropic thermal parameters, correlated motion effects at short distances, and an envelope function which dampens the PDF signal at higher distances as a function of the finite shape and size of nano-sized particles. The instrumental resolution effects on the data were calibrated by fitting the PDF of Ni with a cubic fcc model, and refining the parameters for instrumental dampening and broadening (Q_{damp}= 0.03497 Å^{-1} and Q_{broad} = 0.01614 Å^{-1}).

In order to estimate the range of structural coherence of the samples, we first assumed that the structure of the crystallites is described by the PDF of the bulk crystal, $G_{\text{bulk}}(r)$. After first accounting for the resolution effects, we then additionally modulated the bulk PDF by an envelope function $\gamma_0(r)$ which depends on the size and shape of the crystallite,[59] such that the experimental PDF is then described by the product, as described in Equation 2.

$$G(r) = G_{bulk}(r)\gamma_0(r). \qquad \text{(Eq. 2)}$$

2.3.2. **X-ray photoelectron spectroscopy**

XPS samples were prepared by initially dispersing the nanowire bundle sample in a small amount of ethanol and then depositing multiple small aliquots onto a Si wafer (measuring 1 cm × 1 cm) followed by air drying, so as to ensure complete coverage.

Samples were then transferred into the vacuum chamber of a home-built XPS surface analysis system, furnished with a model SPECS Phoibos 100 electron energy analyzer for electron detection. Once the sample was placed into the chamber, the chamber itself was evacuated to a base pressure of ~$2 \cdot 10^{-10}$ torr. A set of XPS spectra were collected using an Mg Kα X-ray source (hυ = 1253.6 eV) (model XR 50). For data analysis, the C 1*s* peak was set at a position of 284.5 eV[60] in order to subsequently calibrate the relative positions of the Na *1s*, Fe 2*p*, Co 2*p*, and Si 2*p* peaks, respectively. To further analyze the nature of these peaks, the Shirley background was subsequently subtracted, and curve fitting was performed using the XPS PEAK 4.1 software. The software was able to automatically determine accurate positions for the Na *1s*, Fe 2*p*, Co 2*p*, and Si 2*p* peaks upon curve fitting. Finally, the processed data were plotted using the Origin 6.0 software.

2.3.3. **Electron Microscopy**

The morphology and size of the NW bundles were probed using a field emission SEM (FE-SEM Leo 1550) instrument, operating at an accelerating voltage of 15 kV. Both were equipped with EDX capabilities. To prepare these samples for characterization, fixed amounts were dispersed in ethanol and sonicated for ~1 min, prior to their deposition onto the surfaces of silicon (Si) wafers.

Low magnification TEM data were generated at an accelerating voltage of 120 kV on the JEOL JEM-1400 instrument, outfitted with a 2048 x 2048 Gatan CCD digital camera. High-resolution TEM images coupled with SAED patterns were acquired at an accelerating voltage of 300 kV on a JEOL JEM-3000F microscope using a Gatan imaging filter (GIF). Both of these samples had been prepared for analysis by dispersion

in ethanol followed by sonication. Subsequently, the solution was deposited drop-wise onto a 300 mesh Cu grid.

Samples prepared for BET analysis were initially dried in an oven overnight in order to remove any residual solvents. Subsequently, ~100 mg of sample material as well as the corresponding anatase TiO_2 reference standard (i.e. characterized by a surface area of ~10.24 ± 0.54 m^2/g) were placed into an analysis tube. These samples were then subjected to de-gassing for 30 min at room temperature and later for 1 hour at 220°C in order to remove any adsorbed gases that had accumulated onto the particulate surfaces. After de-gassing, the BET surface area analysis was subsequently conducted with a Quantachrome Nova 2200e Series Instrument by using a 10-point sampling method.

2.3.4. **Magnetic Characterization.**

Magnetic data were acquired on powders of as-prepared Co-substituted $NaFeSi_2O_6$ NWs, which had been encapsulated in paraffin wax within a gelatin capsule placed into a plastic straw in order to allow for immersion into the magnetometer. Magnetization measurements were then collected using a Quantum Design Magnetic Property Measurement System (MPMS). Data were acquired at externally applied fields of up to 5 T in magnitude and in the temperature range between 2 and 300 K.

3. Results and Discussion

i. X-ray Diffraction (XRD) & X-ray Photoelectron Spectroscopy (XPS)

In our efforts to reliably generate cobalt-substituted, pyroxene-based NW bundles, control experiments in addition to systematic temperature variations were also initiated in order to more precisely understand the growth mechanism associated with the nanowire

bundles. These sets of runs will be discussed in the following sections as well as in the Supporting Information section (Figures S1-S9). Nonetheless, using the hydrothermal technique, we were able to reproducibly generate Co-substituted $NaFeSi_2O_6$ NW bundles, specifically $NaFeSi_2O_6$ as the underlying structural chemical motif or 'base material', as determined by our synchrotron data (Figure 1). In effect, observable peaks could be assigned to the corresponding COD database standard, i.e. #9005438, for sodium iron silicate as the majority, predominant underlying phase. Moreover, these diffraction patterns could be readily indexed by the structure of monoclinic Aegirine with the space group *C12/c*. XRD reflections associated with the other metal silicate and ferrite standards are compared for reference with our experimental pattern within the Supplementary Information section (Figure S1). From these data, it is evident that the spinel structure clearly does not index the peaks over the wider range measured during the synchrotron experiments, whereas by contrast, aegirine in fact does so, very well.

The NW bundles were further investigated using XPS in order to more accurately determine their chemical composition of the potential crystalline and amorphous material contributions to our systems. Specifically, spectra were collected at binding energies associated with the Fe 2*p*, Co 2*p*, and Si 2*p* transitions, respectively. The accumulated spectra were corrected for charge effects, normalized, and finally subjected to background subtraction. De-convolution of these spectral features was achieved using the XPS PEAK 4.1 software. From the XPS spectra of Co-substituted $NaFeSi_2O_6$, Fe $2p^{3/2}$ peaks located at ~ 728 eV and 714 eV can be likely identified with Fe^{2+} and Fe^{3+}, obtained from iron silicate (Figure 2A).[61] As for the Co spectra (Figure 2B), the presence of Co(II) $2p^{3/2}$ and $2p^{1/2}$ peaks centered at ~799 and ~783 eV, respectively, is indicative of

cobalt silicates.[62,63, 64] Finally, the Si 2*p* peak located at ~104 eV and 105 eV can be ascribed to the formation of SiO_4^{4-}.[63] Additionally, Na peaks were centered within the range of ~1060 to 1070 eV (Figure S2). The results of the XPS spectra correlate well with the XRD data, confirming that the Co-substituted $NaFeSi_2O_6$ phase likely exists as the majority and predominant chemical composition characterizing the nanowire bundles. From these data, it is probable that APTES indeed interacts with the metal ions, thereby forming nanostructured metal silicates.

ii. Electron Microscopy.

The size and the morphology of the Co-substituted $NaFeSi_2O_6$ NWs were observed using FE-SEM and TEM. Representative SEM and TEM images (Figure 3A and B) highlight that the nanostructures possessed the correct morphology and were uniform in size and shape for the Co-substituted $NaFeSi_2O_6$ NWs. Specifically, with the Co-substituted $NaFeSi_2O_6$ NWs (Figure 3A and 3B), SEM and TEM images demonstrated the presence of smooth nanowire bundles, possessing an average length of 5 ± 0.25 μm and an overall width of 250 ± 23 nm. These bundles consisted of individual nanowires, characterized by widths of 2 ± 0.5 nm, based on measurements of ~300 wires in total. It is noteworthy to mention that no significant presence of discrete, isolated individual wires was noticeably apparent within the ferrite samples. In fact, effectively, only bundles of wires were evident.

To further confirm the presence of O, Co, Na, Fe, and Si within the composite Co-substituted $NaFeSi_2O_6$ structure, STEM images along with their corresponding elemental maps are highlighted in Figure 4A-D, wherein we find uniform and homogeneous spatial distributions of the various constituent metallic elements (i.e. Co

and Fe) within these nanowire bundles, as expected. Given the role of the Na^+ in the formation of the apparent nanowire bundles, we probed its presence in our as-produced structures, prepared after 1 hour of reaction. A uniform distribution of Na was observed by means of elemental mapping, as highlighted in Figure S6. Overlap with other elemental profiles indicates that these structures are likely to be homogeneously interspersed with Co, with noticeably lesser amounts (as compared with Na) of this transition metal element present within the bundles. Moreover, we observed a Na peak within the region of the XPS survey spectrum between 1060 to 1070 eV, and according to our XPS analysis, we hypothesize the presence of Co dopant within the overall underlying $NaFeSi_2O_6$ structure.

iii. Magnetic properties

It is important to note that for the NW bundles, the magnetization of the samples did not completely saturate, even in the presence of the largest applied magnetic field of 5 T. This effect is very pronounced for our ultrathin Co-substituted pyroxene NWs at 300 K, which also exhibit an almost linear response, indicative of paramagnetic behavior, due either to reduced interparticle dipole-dipole interactions or to the presence of silicate interspersed within the wires. The incidence of less conductive silicate might have potentially altered the localized electronic environment, associated with the individual Co-substituted pyroxene NW bundles themselves (Figure 5A).[65, 66] This is also a characteristic sign of nanoscale magnetism, which can be attributed to spin canting at the nanowire surface,[67] meaning that the spins are not perfectly aligned. In addition to the low saturation magnetization, the low remanence M_r/M_s present at 5 K suggests the presence of silicate chains within the nanowires themselves. Previous studies have shown

that larger sized SiO_2-$CoFe_2O_4$ core-shell structures gave rise to a similar trend in both the saturation magnetization and the coercivity (H_c), an observation which was attributed to their small nanoparticle size of ~11 nm.[68, 69]

Based upon previous ZFC-FC curves of these metal ferrite materials, particularly the Co series, it was observed that as the particle size decreased, the temperature at which the ZFC and FC curves diverged, i.e. the blocking temperature, T_B,[14] also diminished in magnitude. With the amorphous ultra-small (i.e. 2.6 nm in diameter) particles yielding a T_B of ~45 K,[70] by contrast, our ~2.0 nm crystalline individual NW bundles gave rise to a T_B of ~15 K, above which superparamagnetic behavior is expected (Figure 5B).

iv. PDF Analysis

The experimental PDFs of the Co-substituted pyroxene NWs are plotted in the r-range, up to 60 Å in Figure 6. The PDF peaks diminish quickly as the 'r' values increase, indicating a finite structural coherence within the sample. Due to the broad peaks in the diffraction pattern, there was some ambiguity in indexing the structure in reciprocal space. The presence of sharp peaks in the PDF allowed for a complementary and more sensitive signal by which to test candidate structures. The similarity between the experimental PDF and PDFs simulated (Figure 7) from candidate structures was quantified using the Pearson product-moment correlation coefficient, *P*, defined by Equation 3, as follows

$$P = \frac{1}{1-n}\sum_{i=0}^{n}\left(\frac{x_i-\bar{x}}{\sigma_x}\right)\left(\frac{y_i-\bar{y}}{\sigma_y}\right) \qquad \text{(Eq. 3)}$$

wherein $\bar{x}$ and $\bar{y}$ are the mean values and σ_x and σ_y are the standard deviations of the respective datasets 'x' and 'y'. The calculation gives a value of *P* between -1 and 1,

wherein 1 implies perfect correlation, 0 implies no correlation, and -1 suggests perfect anti-correlation. Higher positive *P* values typically indicate a higher degree of structural similarity. In effect, the most plausible structure candidates can be identified through comparisons which yield the largest *P* value, typically in the range of 0.8 or higher.[71, 72] We tested a wide range of potential structures (Table S1), and found that the pyroxene-type structure of Aegirine not only gave rise to the only reasonable *P* value but also yielded a very high correlation value of 0.92.

We initially fit the experimental data with the Aegirine structure over a range of 1.0 to 25.0 Å. Without initially allowing for refinement of the atomic positions, we obtained a resulting R_w ~0.30. To calculate the limit of how well this crystallographic structure could fit the experimental data, we then systematically allowed for atomic positions to refine by means of symmetry with first the metal/silicon sites, giving R_w ~0.27, and then both metal/silicon and oxygen sites, yielding R_w ~0.25. Use of anisotropic thermal parameters provided for limited improvement. Additionally, we attempted a refinement which allowed for Fe to 'dope' onto Na sites and another analogous refinement, which analogously permitted Co to 'dope' onto Fe sites. In the former case, the agreement factor went up slightly upon adding Fe, which seems to indicate that there is not significant doping of Fe for Na. In the latter case, there was little deviation in agreement. The similarity in the scattering power between Fe and Co suggests that we cannot easily distinguish between these two elements using this model.

Lastly, given that the dampening of the PDF signal for a spherical crystallite does not fit the PDF envelope of the NWs well over a high 'r'-range, we used the Diffpy-CMI complex modeling software[73] to simulate the NW PDF over a wider range of 1.0-40.0 Å.

Our protocol utilized a spheroidal shape function in which the polar radius was assumed to be infinitely long, and the equatorial radius was allowed to refine. The net result of this analysis was that we obtained an approximate value of 3 nm for the nanowire width, a finding which agrees well with TEM results. The resulting fit (with metal/silicon sites refined) is shown in Figure 7, and the accompanying data are provided in Table 2. The fits are very satisfactory, yielding high confidence that this model is correct for describing the structure of the NWs.

Overall, the residual misfit leftover in the refinement could indicate a few different things. In general, our model does not take into account the variety of either possible doping or surface defects. There is also the possibility of lower local symmetry as well as the presence of either other phases or phase distributions, which are not well described by a single structure. This finding supports our complementary EDX and XPS results which seem to show that there may be some segregation of Co-rich regions.

v. Plausible Growth Mechanism

Systematic variations in a number of reaction parameters such as temperature and time were employed to better understand the growth formation of pyroxene nanowire bundles including varying base (such as using either KOH or NH_4OH instead of NaOH) as well as the presence of ionic additive species (Supplementary Information section, Figures S3-S9). We focus on other more significant parameters herein.

For example, to study the *temperature dependence* for the formation of Co-substituted $NaFeSi_2O_6$ bundles, the reaction temperature was increased in 20 degree intervals up to a nominal reaction time of 6 hours. TEM images of the as-prepared structures collected at various synthesis temperatures are shown in Figure 8. From this

study, it was observed that, at 180°C (Figure 8A), a nebulous strand-like coating appeared to surround and coat our as-prepared, ultra-small amorphous nanoparticles. Generally at this temperature, the adsorption of APTES takes place through a dehydration process, wherein water molecules present in the reaction medium react with the ethoxy groups forming either silanols or linear silicate chains sharing oxygen atoms.[34] As the temperature is increased to 200°C, as shown in Figure 8B, nanoparticle aggregation and accompanying nanoscale strands were observed, features which could be potentially ascribed to the formation of metal ion seeds (i.e. based on Co and/or Fe) and linear silicate chains, respectively. Nonetheless, these processes are suggestive of the occurrence of initial seed nucleation followed by particulate fusion into 1D strands.

It is plausible to hypothesize that the negatively charged silicate strands are electrostatically stabilized by the combination of positively charged Na^+ and metal cations in solution, associated with NaOH and the relevant transition metal precursors.[74] As the temperature was further increased to 220°C (Figure 8C), well-defined, crystalline NW bundles of presumably pyroxenes were observed. Moreover, residual silicate present within the reaction medium likely facilitated the formation of the bundles.

In parallel, a reaction *time-dependent* study was conducted at a fixed reaction temperature of 220°C. These efforts focused on further understanding the roles of both sodium hydroxide and APTES in enabling and facilitating the transformation of nanoparticles to nanowire bundles for the Co-substituted $NaFeSi_2O_6$ species. Hence, the concept was that the presence of sodium hydroxide (NaOH) would assist in and perhaps enable the eventual synthesis of our Co-substituted $NaFeSi_2O_6$ NW bundles. The time-dependent study began at 3 h, as crystalline materials were initially created at that time.

After 3 hours at 220°C, nanoparticle aggregates were observed for the $NaFeSi_2O_6$ base material, as shown in Figure 9A. As the reaction time was additionally increased to 4 hours, the initial formation of nanoparticle aggregates evolved into the production of increased numbers of nanoscale strands (Figure 9B). Finally, by 5 h of reaction time, as shown in Figure 8C, these nanoparticles had transformed and coalesced into more ordered and structured nanoscale strands of pyroxenes, assembled within a perceptible framework. This degree of organization increased with ever greater reaction times, i.e. 6 h, thereby resulting in the formation of recognizable NW bundles. Additionally, infrared spectroscopy (Figure S8) was used to track changes to the Si-O bonding motifs, wherein a more complex hierarchical network-like bonding and assemblage of NW bundles was eventually observed, as discussed in the Supplementary Information section.

The underlying role of pH should not be minimized. It is well known that the presence of a basic environment is mechanistically central and moreover, critical to the nucleation, the rate of growth, and ultimately, the size and morphology of the isolated product. Typically for metal oxide species, under high pH conditions, nucleation rates increase, thereby initially forming hydroxides (as shown in Equation 4) that at the outset, likely form as small nanoparticulate seeds.[75, 76]

$$CoCl_2 + FeCl_3 + 5\ NaOH \rightarrow Co(OH)_2 + Fe(OH)_3 + 5\ NaCl \qquad \text{(Eq. 4)}$$

In the case of our nanowires, high pH conditions (i.e. pH 8-13) strongly influence the transport behavior of the constituent metal ion ‘seeds’ and likely stabilize the growth and formulation of larger, monolithic structures. It is likely that the constituent sodium ions and metal ion ‘seeds’ dissociated within the aqueous solution medium were able to localize and recombine within the spatial framework of NW bundles. Such a scenario is

consistent with our formation of Co-substituted $NaFeSi_2O_6$ NW bundles under pH 9 conditions.[77, 78] Indeed, high pH conditions promote hydrolysis and dehydration processes within the reaction vessel, thereby inducing metal silicate nucleation.[79]

Hence, based upon the combined temperature and time-dependent reaction studies under alkaline conditions, we can reasonably postulate that the predominant reaction mechanism herein involves an initial nucleation followed by aggregation and subsequent recrystallization to yield the resulting NWs. That is, first, the bulky precipitate from the metal and surfactant precursors dissolve in water, forming smaller, more numerous and discrete, and relatively homogeneous metal silicate seeds (Figure 10A). These individual seeds then cluster and coalesce together to form sheets (Figure 10B). This process presumably occurs through an oriented attachment mechanism, which would account for the formation of anisotropic structures through collisions and coalescence of smaller particles to form larger structures as a result of either favored crystallographic or surface orientations.[80]

Subsequently, the silicate seeds may form straight chain-like structures consisting of repeating silicate molecules, wherein dangling oxygen atoms undergo charge compensation in the presence of surrounding sodium and metal ions. It is also worth mentioning that the existence of ionic channels for sodium has been demonstrated by using inelastic neutron scattering within sodium silicate structures and that furthermore, the Si-O network remains otherwise inert.[81] Hence, this ionic and relatively conducting oxide 'supporting framework' may enable the local inclusion of transition metal cations, i.e. Na, Fe, and Co. It is plausible therefore that the presence of adjacent vacancies may thereby favorably facilitate the formation of interfacial phases, such as $NaFeSi_2O_4$.

Specifically, positively charged Na^+ and transition metal cations can cluster together, and electrostatically neutralize negatively-charged linear silicate chains, in so doing, stabilizing them and facilitating the formation of strand-like structures comprised of repeating silicate molecules (Figure 10C).[82] It is then presumed that the simultaneous presence of APTES within the reaction medium may (i) assist in the stabilization of these nanostrands, (ii) enable their continued anisotropic growth, and (iii) subsequently ease their transformation into clusters of 1D NWs, stacked into more complex bundle-like configurations (Figure 10D).[83]

Similar behavior has been observed by Manjunatha *et al.*, associated with the preparation of $CdSiO_3$ nanobelts via a hydrothermal method.[74] Specifically, both their $CdSiO_3$ and our own $NaFeSi_2O_4$ nanowires herein employ a silicate precursor as a template to yield a linear straight chain with metal ions stabilizing this chain, thereby forming 'sandwich structures' composed of alternating silicate and metal layers stacked one above the other.[74] However, Manjunatha *et al.* did not observe a synergistic interaction between the silicate and Na^+ ions nor did they attribute the presence of Na^+ ions to the possibility of influencing the observed nanowire morphology, even though the silica source for the $CdSiO_3$ nanobelts was indeed sodium metasilicate (Na_2SiO_3). Nevertheless, based upon observations from the previous literature as well as from our own insights collected herein, a time evolution of nanowire formation is highlighted and summarized in our growth schematic, depicted in Figure 10.

What is unique about our proposed formation mechanism is that we highlight the constructive and synergistic role of NaOH in terms of favorably promoting nanowire growth. Specifically, to further confirm our hypothesis concerning the synergistic effects

of APTES and NaOH for nanowire growth, control experiments were performed in the absence of either APTES or NaOH precursors. These runs yielded primarily nanoparticles and of a different and undesirable chemical composition. Specifically, control experiments in the absence of NaOH were performed exclusively in water as well as in mixed water: ethanol (1:1 v/v) solutions. Interestingly, after 6 hours in aqueous solution, nanowires began to form from the bulk-like precursors. Nevertheless, as the reaction time progressed from 6 to 24 hours, these Fe_3O_4 nanowires began to degrade into ultra-small nanoparticles (Figure S3 A-C).

Indeed, the implication is that APTES can induce the formation of linear chains. However, in the absence of basic conditions, i.e. in the absence of Na^+ ions for example, this linear template is not stabilized and the metal precursor seeds end up forming nanoparticles. Based upon time-dependent studies, this type of scenario played out in an aqueous water-ethanol solution, as initially the metal silicates had formed small but discernible 1D building blocks circumferentially coated with ultra-small nanoparticles after 6 hours of reaction.

Though it is certainly possible that crystal splitting of these rectangular blocks into nanowires could occur at longer reaction times, we instead observed the formation of discrete nanoparticles (Figure S3 D-F). These observations confirm the significance and the necessity of the simultaneous presence of both APTES and NaOH in bringing about the growth of anisotropic nanowires of Co-substituted $NaFeSi_2O_4$ in our systems. To this end, we note the presence of Na and Si within the 1D structures we created, using elemental mapping techniques, with the data shown in the Supporting Information (Figure S7).

Surfactant-assisted growth protocols are common in the context of 1D materials, and are well understood.[49, 84-87] However, it is worth reinforcing that although APTES as the surfactant is definitely a major contributor to our nanowire bundle motif, we consider the presence of ionic species to be equally important determinants of the resulting morphology as well. Indeed, previous reports have indicated that Na^+ ions can preferentially adsorb onto a particular facet and thereby promote[88-90] one-dimensional growth within metal oxide systems.[15,16] Herein, we propose constructive and beneficial synergistic interactions between the APTES surfactant and the Na^+ metal cation, as essential and critical factors driving the nanowire growth of Co-substituted $NaFeSi_2O_4$.

This concept of positive synergy between surfactants and metal ions and its resulting directing influence upon crystal growth has been previously documented. For example, the simultaneous presence of both cetyltrimethylammonium bromide (CTAB) and Ag^+ ions enabled Au nanorod growth,[91] whereas the concurrence of both Ca^{2+} and CTAB allowed for the generation of highly faceted iron oxides.[92] From our control experiments, given the introduction of Na^+ ions from the basic solution used, it is therefore feasible to envision a mutually complementary and synergistic interaction between APTES and the ions in solution with respect to nanowire formation. To further bolster this point, we explored the specific effect of using various different bases and counter-ion sizes in analyzing the resulting nanowire growth. The resulting data and conclusions are presented and summarized in the Supplementary Information section.

vi. Role of Silicate Derivatives

To gain further mechanistic insights, we varied the identity of the silica source used. Specifically, we sought alternatives to APTES, such as tetraethoxysilane (TEOS)

and tetramethoxysilane (TMOS), possessing similar silicate groups in order to confirm the role of this particular surfactant in the observed nanowire growth. APTES is a surfactant-like molecule maintaining a silicate SiO_3^{2-} head group in addition to an amine-terminated functional group, which can exist as a positively charged species under lower pH conditions. Our high pH, basic reaction conditions likely rule out that there are charged amines that may be either contributing to the formation of either electrostatic complexes or acting as facet-capping agents. Hence, we hypothesize that the silicate head group within APTES plays a role in directing morphology.

To further rule out the effect of the amine functional group, 'amine-less' species, i.e. TEOS and TMOS, were substituted for APTES (Figure 11A). The net result of these experiments was that we observed similar wire-like bundle morphologies by TEM (Figures 11B and 11C). These results corroborate the role of the silicate functional groups in directing the resulting overall crystal growth.

4. Conclusions

We have synthesized crystalline Co-substituted sodium iron silicate nanowire bundles, using a readily scalable hydrothermal method. The silicate may either be coating the nanowires themselves or interspersed between the bundles, although evidence for the latter scenario is likely stronger. The roles of various precursors were probed in an effort to understand their respective roles in nanowire growth. Hence, based upon control experiments, such as (i) the absence of either APTES or NaOH precursors, (ii) the substitution of APTES with TEOS and TMOS silicate derivatives, as well as (iii) the substitution of NaOH with KOH and NH_4OH, we conclude that the simultaneous

presence of both APTES surfactant and NaOH is critical for enabling the observed nanowire bundle growth.

Hence it is reasonable to assert that a positive and constructive synergistic effect exists between APTES and NaOH and that favorable interactions between the two can favorably control nanowire growth. Specifically, we postulate that the presence of both Na^+ and metal precursor cations neutralize the dangling oxygen atoms on the linear chain template induced by the presence of the APTES surfactant.

PDF results indicate that the NW bundles most closely resemble the pyroxene type structure, Aegirine. The overall observed fit agreement within the range of R_w = 0.25-0.30, depending on model parameters, is fairly good for such a complicated nanomaterial. We expect that the misfit may have resulted from unaccounted defects in addition to the possibility of lowered local symmetry as well as to the presence of other phases or phase distributions. SQUID measurements suggest not only superparamagnetic behavior at 5 K but also paramagnetic behavior at 300 K for the series of Co-substituted $NaFeSi_2O_4$ NWs. These magnetic data resemble that of ultra-small nanoparticles, a finding which can possibly be ascribed to the presence of silicates interspersed within the nanowire bundles. In effect, the presence of the silicate might have altered the localized electronic environment probed within the NWs themselves.

5. Acknowledgements

Funds for research work (including support for all authors) at Brookhaven National Laboratory (BNL) were provided by the U.S. Department of Energy, Office of Basic Energy Sciences, Materials Sciences and Engineering Division under Contract No.

DE-SC-00112704. High-resolution electron microscopy data in this manuscript were collected in part at BNL's Center for Functional Nanomaterials, which is also supported by the U.S. Department of Energy under Contract No. DE-SC-00112704. X-ray PDF measurements were conducted at beamline 28-ID-2 of the National Synchrotron Light Source II, a U.S. Department of Energy (DOE) Office of Science User Facility operated for the DOE Office of Science by Brookhaven National Laboratory under Contract No. DE-SC0012704. We thank Eric Dooryhee and A.M. Milinda Abeykoon in particular for their technical assistance and guidance in data acquisition.

6. Supporting Information Available. Mechanistic details as well as additional XRD, TEM, STEM, and infrared spectroscopy data. This information is available free of charge via the Internet at http://pubs.acs.org.

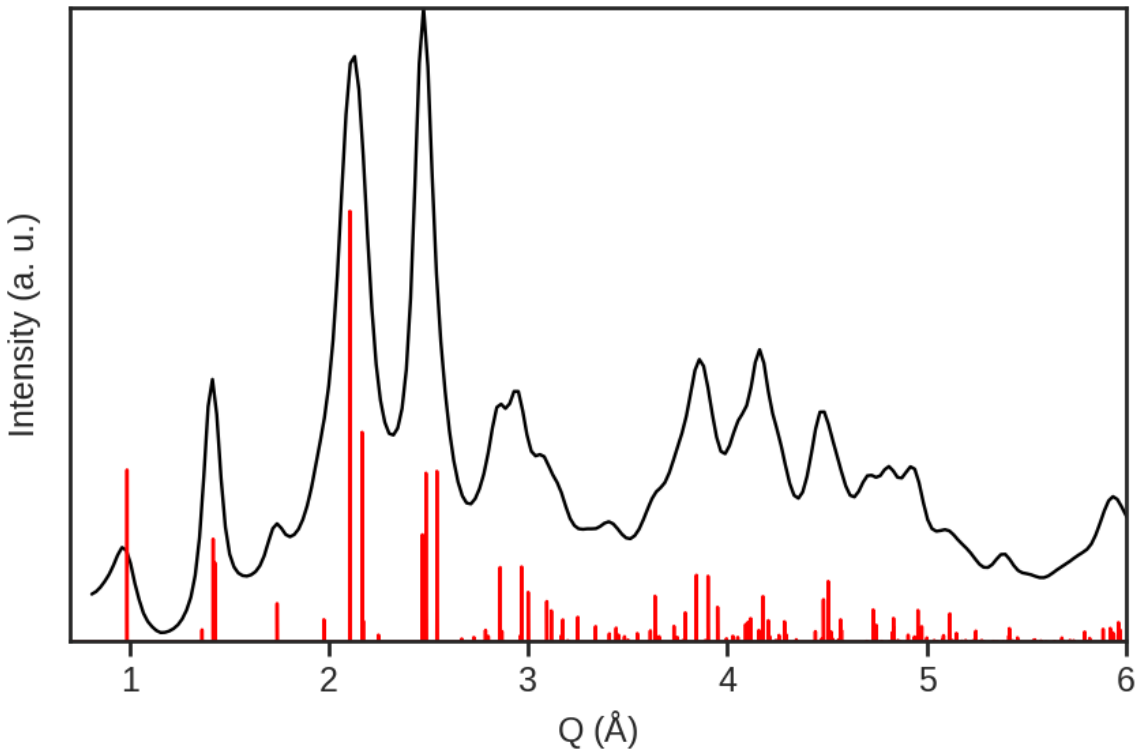

Figure 1. XRD pattern (black) of as-prepared Co-substituted $NaFeSi_2O_6$ bundles, generated via a hydrothermal method. The COD standard (# 9005438) used to index the underlying Aegirine crystal structure is shown in red.

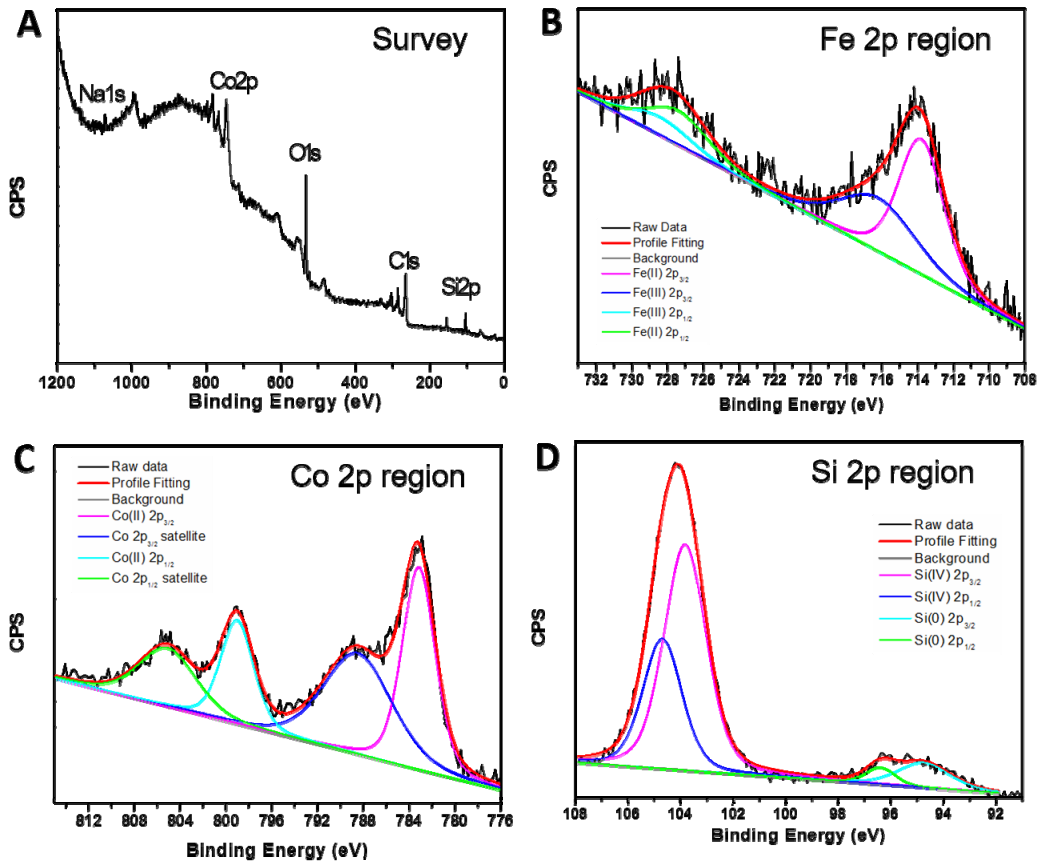

Figure 2. X-ray photoelectron spectroscopy data of Co-substituted $NaFeSi_2O_6$ nanowire bundles. (A) Whole survey spectrum, including regions associated with Na *1s* as well as (B) Fe 2*p*, (C) Co 2*p*, and (D) Si 2*p*, respectively. The de-convolution of each of the accumulated spectra implies the presence of Fe silicates, Co silicates, as well as the silicate group SiO_4 itself, respectively.

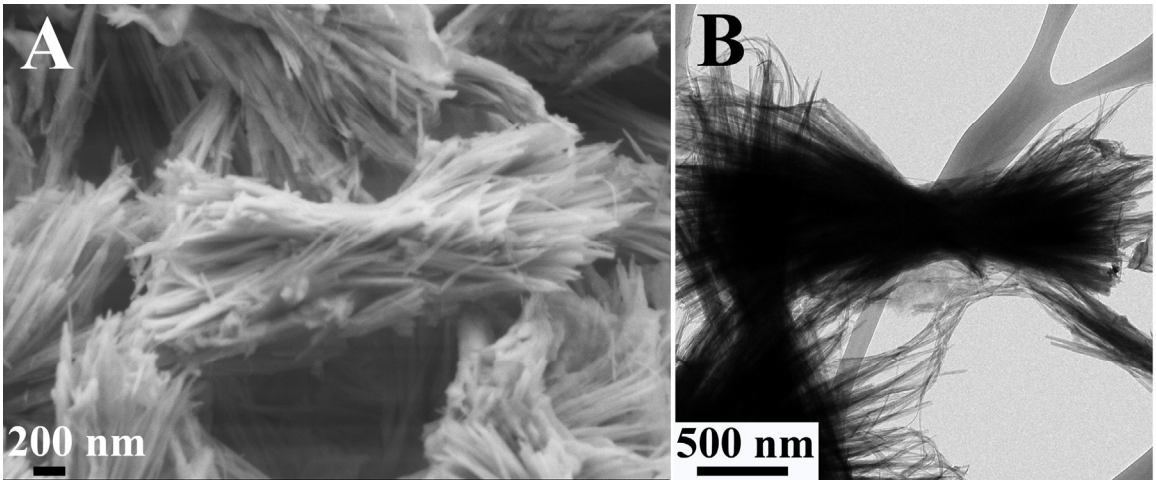

Figure 3. Representative (A) SEM and (B) TEM images of as-prepared Co-substituted $NaFeSi_2O_6$ NW bundles

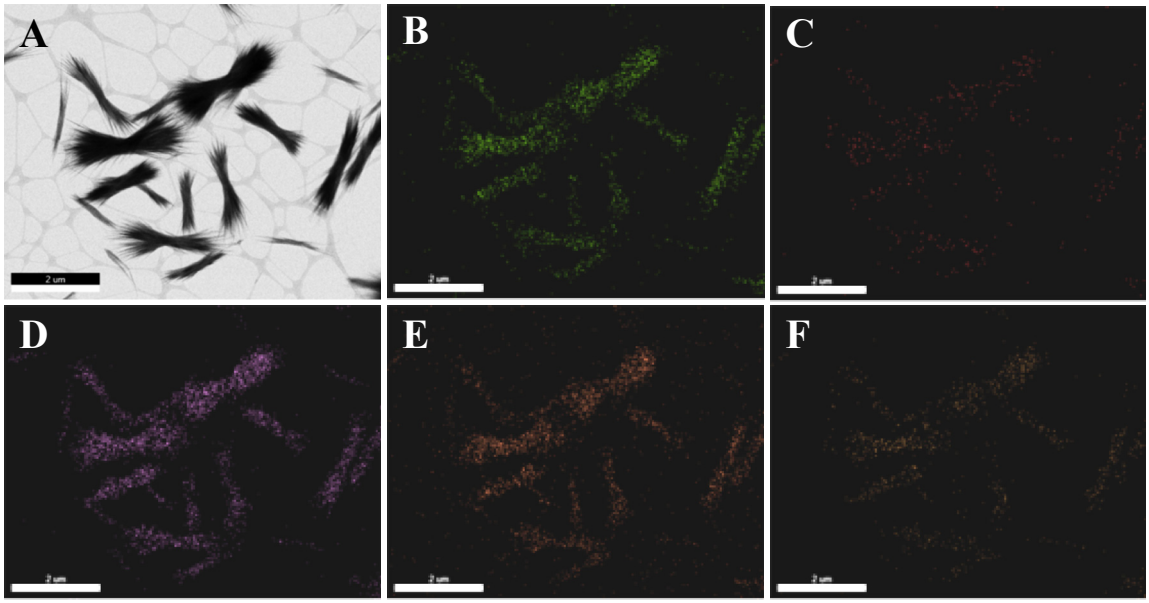

Figure 4. STEM image of as-prepared Co-substituted $NaFeSi_2O_6$ NWs. EDS mapping highlights the elemental spatial distributions of O, Co, Si, Fe, and Na, respectively. Scale bar is 2 μm.

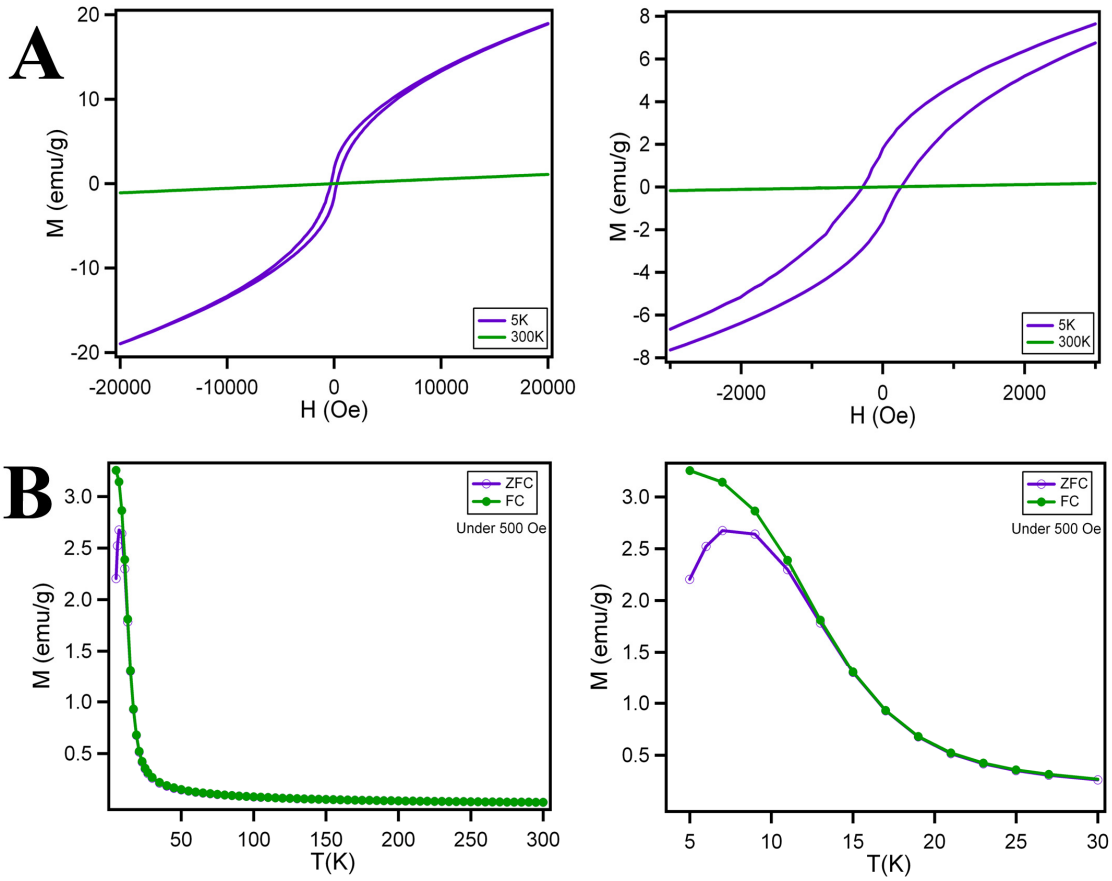

Figure 5. M versus H curves (A) at 5 K and 300 K with ZFC-FC curves (B) with an applied field of 500 Oe for the Co-substituted $NaFeSi_2O_6$ NWs.

Table 1. Magnetic characterization and surface area of Co-substituted $NaFeSi_2O_6$ NWs. Magnetic characterization data were obtained from M versus H curves at 5 K and 300 K, along with ZFC-FC curves at an applied field of 500 Oe. Note the unit (emu/g) is calculated for the total mass of the material.

Name	**T (K)**	**H_c (Oe)**	**M_s (emu/g)**	**M_R (emu/g)**	**M_r/M_s**	**T_{max}/T_B (K)**	**BET surface area (m^2/g)**
Co-substituted $NaFeSi_2O_6$	5 300	330 ---	16.5 2.5	1.8 ---	9.1 ---	15	52.79

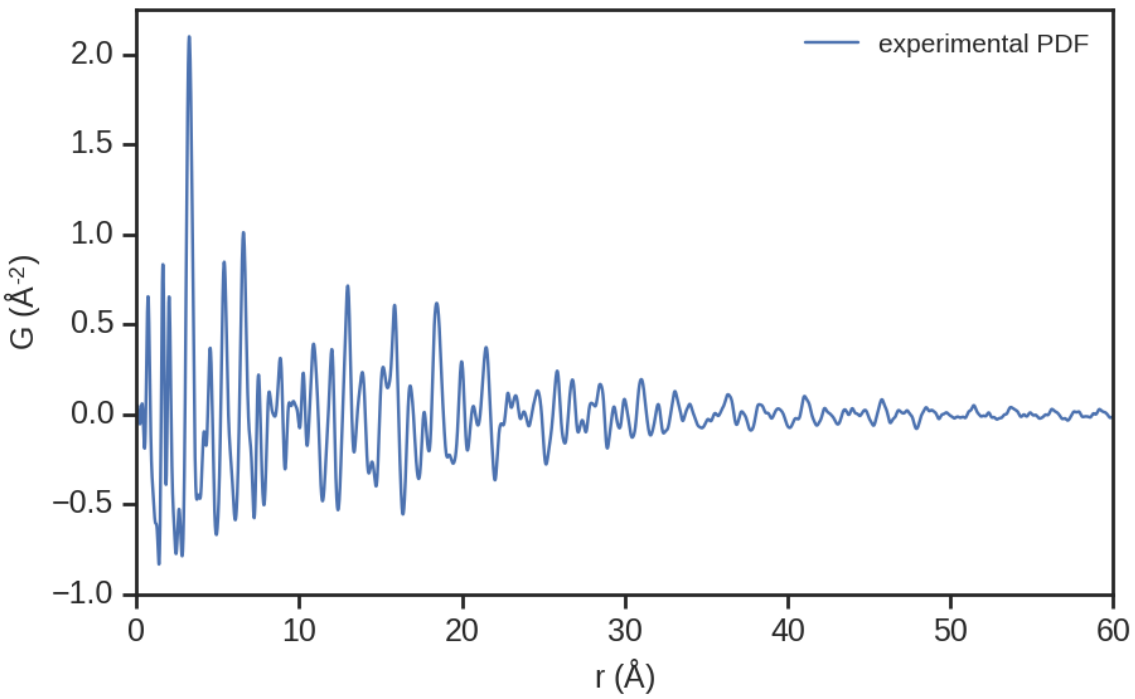

Figure 6. Measured PDF profile for Co-substituted $NaFeSi_2O_6$ NW bundles, plotted in an 'r'-range of up to 40 Å.

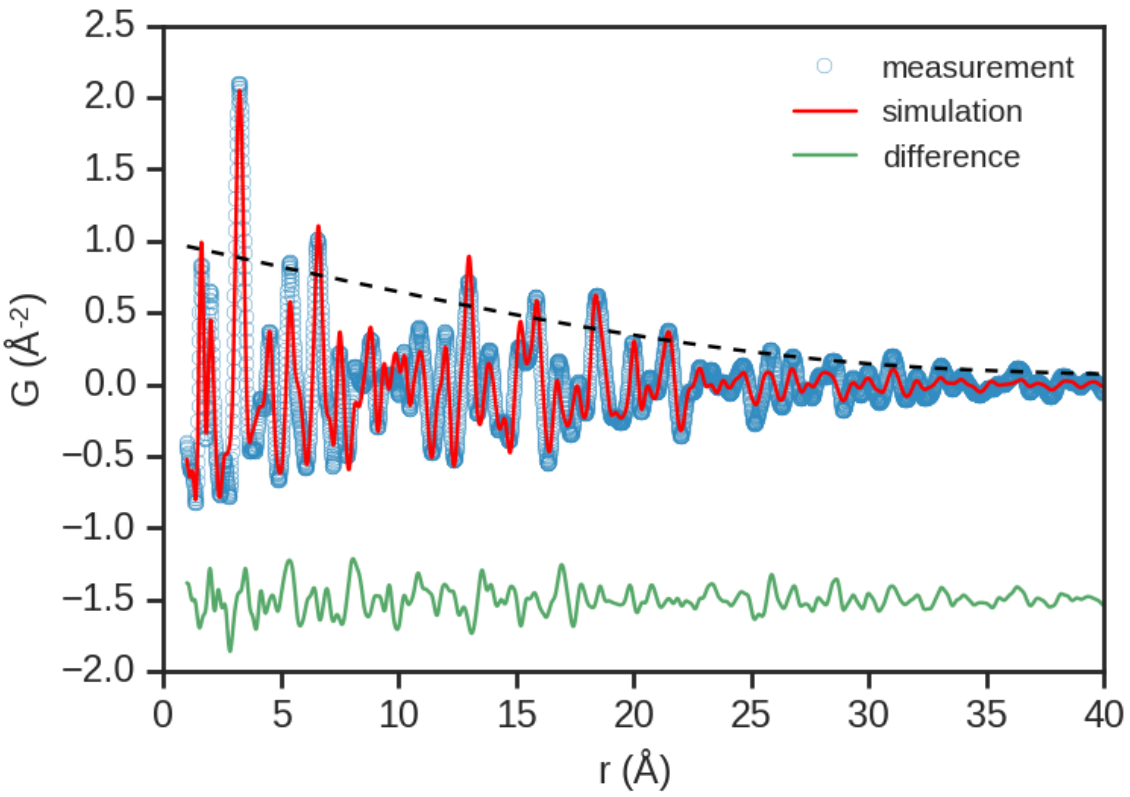

Figure 7. PDF fits for as-prepared Co-substituted $NaFeSi_2O_4$ NW bundles in an 'r'-range from 1 Å to 40 Å. The blue circles and red solid line correspond to measured and simulated PDFs, respectively. The green solid line offset below denotes the difference curve, and the black dashed line represents the envelope function for a wire, simulated by a prolate spheroid with infinite length and finite equatorial diameter.

Table 2. Resulting fit parameter values from refinement of the Aegirine structure to the $NaFeSi_2O_6$ NW bundles, using the spheroidal envelope function, over a range of 1.0 to 40.0 Å.

	$NaFeSi_2O_6$ NW Bundles
a (Å)	9.71
b (Å)	8.81
c (Å)	5.32
β (°)	107.48
Wire width (Å)	30
y (Na)	0.277
y (Fe)	0.897
x (Si)	0.287
y (Si)	0090
z (Si)	0.225
U_{iso} (Na) ($Å^2$)	0.024
U_{iso} (Fe) ($Å^2$)	0.008
U_{iso} (Si) ($Å^2$)	0.012
U_{iso} (O) ($Å^2$)	0.025
R_w	0.28

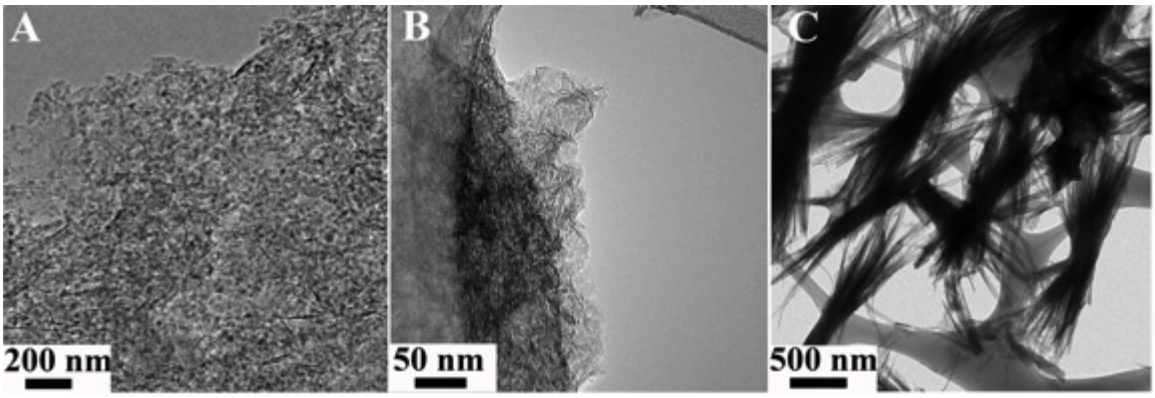

Figure 8. Representative TEM images of Co-substituted $NaFeSi_2O_6$ NW bundles, synthesized at (A) 180°C, (B) 200°C, and (C) 220°C, respectively.

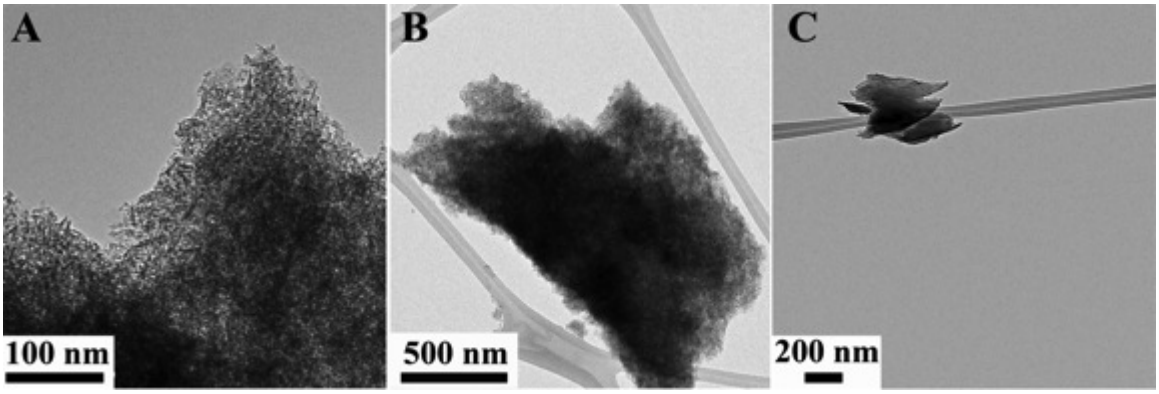

Figure 9. Representative images concerning the time evolution of the (A, B, and C) Co-substituted pyroxene-based nanostructures, associated with reaction time intervals of (A) 3 h, (B) 4 h, and (C) 5 h, respectively.

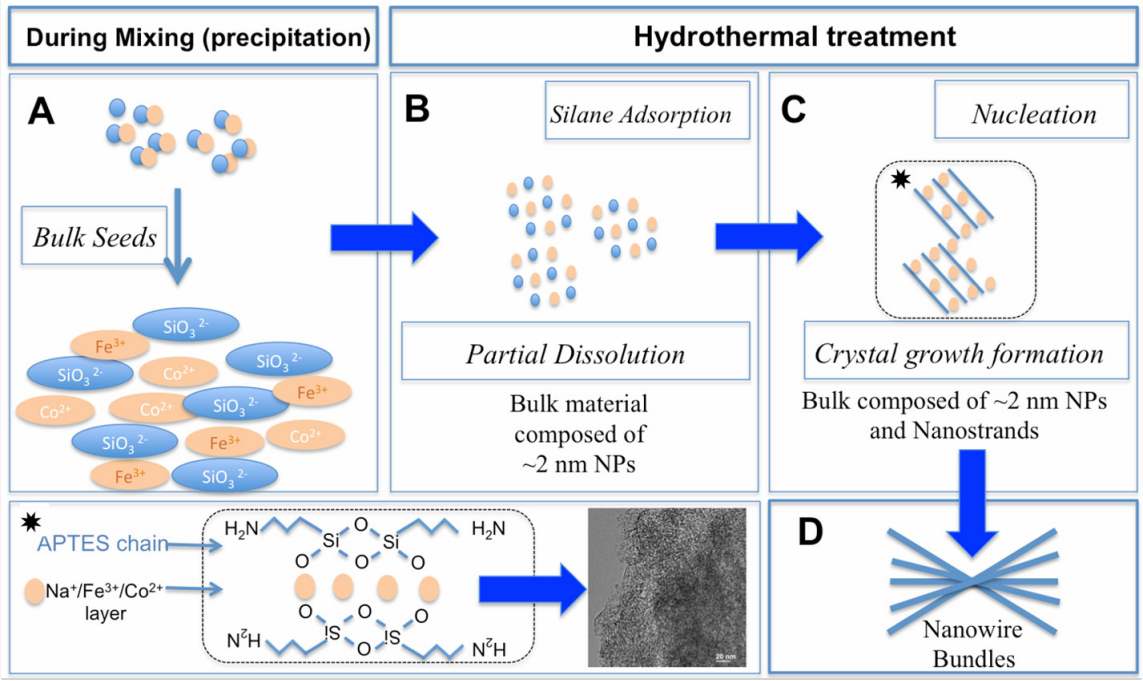

Figure 10. A modified schematic representation for the proposed growth mechanism of Co-substituted pyroxene nanowire bundles, as suggested by Manjunatha et al. *J. Mater. Chem*. **2012**, v.22, pp. 22392-22397. A magnified image of the proposed nucleation process within panel C is designated by an asterisk.

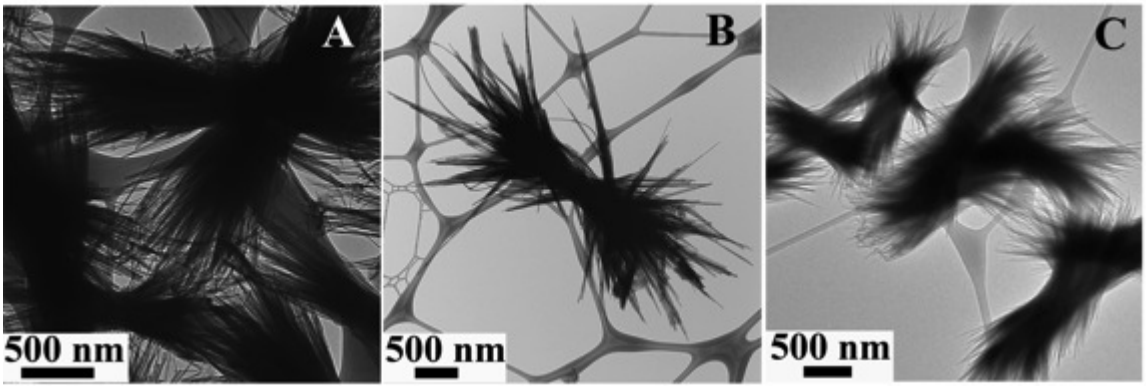

Figure 11. As-prepared Co-substituted pyroxene nanowire bundles, created using various silica sources, such as (A) aminopropyltriethoxy silane (APTES), (B) tetraethyl orthosilicate (TEOS), and (C) tetramethyl orthosilicate (TMOS), respectively.

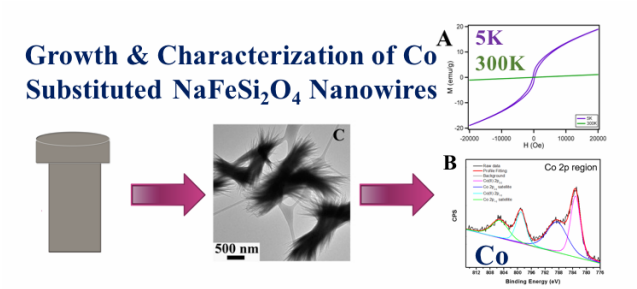

TOC Figure Caption. We report on the synthesis and mechanistic study of Co-substituted pyroxene nanowires of controllable dimensions and their subsequent correlation with magnetic properties.

References

1. J. L. Moran-Lopez, R. A. Guirado-Lopez, J. M. Montejano-Carrizalez, F. Aguilera-Granja, R. Rodriguez-Alba, J. Mejia-Lopez, A. H. Romero and M. E. Garcia, *Current Science*, 2008, **95**, 1177-1201.
2. A. K. M. Bantu, J. Rivas, G. Zaragoza, M. A. López-Quintela and M. C. Blanco, *Journal of Applied Physics*, 2001, **89**, 3393-3397.
3. J. P. Pierce, E. W. Plummer and J. Shen, *Journal of Applied Physics Letters*, 2002, **81**, 1890-1892.
4. F. Zighem, T. Maurer and F. Ott, *Journal of Applied Physics*, 2011, **109**, 013910-013911-013910-013918.
5. M. Ravichandran, G. Oza, S. Velumani, J. T. Ramirez, F. Garcia-Sierra, N. B. Andrade, M. A. Garza-Navarro, D. I. Garcia-Gutierrez, R. Lara-Estrada, E. Sacristán-Rockf and J. Yig, *RSC Advances*, 2015, **5**, 17223-17227.
6. S. Zeng, D. Baillargeat, H.-P. Ho and K.-T. Yong, *Chemical Society Reviews*, 2014, **43**, 3426-3452.
7. Z. Wang, X. Liu, M. Lv, P. Chai, Y. Liu, X. Zhou and J. Meng, *The Journal of Physical Chemistry C*, 2008, **112**, 15171-15175.
8. D. A. Allwood, G. Xiong, M. D. Cooke, C. C. Faulkner, D. Atkinson, N. Vernier and R. P. Cowburn, *Science*, 2002, **296**, 2003-2006.
9. A. Manzoor, A. M. Afzal, M. Umair, A. Ali, M. Rizwan and M. Z. Yaqoob, *Journal of Magnetism and Magnetic Materials*, 2015, **393**, 269-272.
10. J. L. Ortiz-Quinonez, D. Diaz, I. Zumeta-Dube, H. Arriola-Santamaria, I. Betancourt, P. Santiago-Jacinto and N. Nava-Etzana, *Inorg Chem*, 2013, **52**, 10306-10317.
11. J. M. Patete, J. Han, A. L. Tiano, H. Liu, M.-G. Han, J. W. Simonson, Y. Li, A. C. Santulli, M. C. Aronson, A. I. Frenkel, Y. Zhu and S. S. Wong, *Journal of Physical Chemistry C*, 2014, **118**, 21695-21705.
12. T.-J. Park, G. C. Papaefthymiou, A. J. Viescas, A. R. Moodenbaugh and S. S. Wong, *Nano Letters*, 2007, **7**, 766-772.
13. T.-J. Park and S. S. Wong, *Chemistry of Materials*, 2006, **18**, 5289-5296.
14. A. L. Tiano, G. C. Papaefthymiou, C. S. Lewis, J. Han, C. Zhang, Q. Li, C. Shi, A. M. M. Abeykoon, S. J. L. Billinge, E. Stach, J. Thomas, K. Guerrero, P. Munayco, J. Munayco, R. B. Scorzelli, P. Burnham, A. J. Viescas and S. S. Wong, *Chemistry of Materials*, 2015, **27**, 3572–3592.
15. K. Bergum, H. Okamoto, H. Fjellvag, T. Grande, M. A. Einarsrud and S. M. Selbach, *Dalton Transactions*, 2011, **40**, 7583-7589.
16. A. Pui, D. Gherca and N. Cornei, *Materials Research Bulletin*, 2013, **48**, 1357-1362.
17. C. Pereira, A. M. Pereira, C. Fernandes, M. Rocha, R. Mendes, M. P. Fernández-García, A. Guedes, P. B. Tavares, J.-M. Grenèche, J. P. Araújo and C. Freire, *Chemistry of Materials*, 2012, **24**, 1496-1504.
18. H. Zhao, H. Jia, S. Wang, D. Xue and Z. Zheng, *Journal of Experimental Nanoscience*, 2011, **6**, 75-83.
19. E.-K. Lim, Y.-M. Huh, J. Yang, K. Lee, J.-S. Suh and S. Haam, *Advanced Materials*, 2011, **23**, 2436-2442.

20. J.-T. Jang, H. Nah, J.-H. Lee, S. H. Moon, M. G. Kim and J. Cheon, *Angewandte Chemie*, 2009, **121**, 1260-1264.
21. J. Li, Y.-L. An, F.-C. Zang, S.-F. Zong, Y.-P. Cui and G.-J. Teng, *Journal of Nanoparticle Research*, 2013, **15**, 1-10.
22. H. Joshi, *Journal of Nanoparticle Research*, 2013, **15**, 1-19.
23. M. Cao, P. Wang, Y. Kou, J. Wang, J. Liu, Y. Li, J. Li, L. Wang and C. Chen, *ACS Applied Materials & Interfaces*, 2015, **7**, 25014-25023.
24. M. Luo, C. Dai, Q. Han, G. Fan and G. Song, *Surface and Interface Analysis*, 2016, **48**, 1066-1071.
25. A. Pourjavadi, Z. M. Tehrani and A. Shakerpoor, *Supramolecular Chemistry*, 2016, **28**, 624-633.
26. P. Esmaeilnejad-Ahranjani, M. Kazemeini, G. Singh and A. Arpanaei, *Langmuir : the ACS journal of surfaces and colloids*, 2016, **32**, 3242-3252.
27. I. Sarvi, Gholizadeh, M. & Izadyar, M. , *Catalysis Letters*, 2017, **147**, 1162-1171.
28. Y. Wang, Y. Sun, J. Wang, Y. Yang, Y. Li, Y. Yuan and C. Liu, *ACS Applied Materials & Interfaces*, 2016, **8**, 17166-17175.
29. N. R. Jana, C. Earhart and J. Y. Ying, *Chem. Mater.*, 2007, **19**, 5074-5082.
30. I. Koh, X. Wang, B. Varughese, L. Isaacs, S. H. Ehrman and D. S. English, *The Journal of Physical Chemistry B*, 2006, **110**, 1553-1558.
31. D. Liu, A. M. Pourrahimi, L. K. H. Pallon, R. L. Andersson, M. S. Hedenqvist, U. W. Gedde and R. T. Olsson, *RSC Advances*, 2015, **5**, 48094-48103.
32. A. Parodi, N. Quattrocchi, A. L. van de Ven, C. Chiappini, M. Evangelopoulos, J. O. Martinez, B. S. Brown, S. Z. Khaled, I. K. Yazdi, M. V. Enzo, L. Isenhart, M. Ferrari and E. Tasciotti, *Nature Nanotechnology*, 2013, **8**, 61-68.
33. U. Sakulkhu, M. Mahmoudi, L. Maurizi, G. Coullerez, M. Hofmann-Amtenbrink, M. Vries, M. Motazacker, F. Rezaee and H. Hofmann, *Biomaterials Science*, 2015, **3**, 265-278.
34. Z. Liu, X. Duan, G. Qian, X. Zhou and W. Yuan, *Nanotechnology*, 2013, **24**, 045609/045601-045609/045606.
35. A. E. Ringwood, *Geochimica et Cosmochimica Acta*, 1991, **55**, 2083–2110.
36. W. L. Mao, Y. Meng, G. Shen, V. B. Prakapenka, A. J. Campbell, D. L. Heinz, J. Shu, R. Caracas, R. E. Cohen, Y. Fei, R. J. Hemley and H. K. Mao, *Proceedings of the National Academy of Sciences*, 2005, **102**, 9751-9753.
37. H.-k. Mao, G. Shen and R. J. Hemley, *Science*, 1997, **278**, 2098.
38. R. M. Hazen, *American Mineralogist*, 1977, **62**, 286.
39. M. C. Aronson, L. Stixrude, M. K. Davis, W. Gannon and K. Ahilan, *American Mineralogist*, 2007, **92**, 481.
40. S. Jodlauk, P. Becker, J. A. Mydosh, D. I. Khomskii, T. Lorenz, S. V. Streltsov, D. C. Hezel and L. Bohaty, *Journal of Physics: Condensed Matter*, 2007, **19**, 432201/432201-432201/432209.
41. S. W. Cheong and M. Mostovoy, *Nat Mater*, 2007, **6**, 13-20.
42. W. Lottermoser, R. Müller and H. Fuess, *Journal of Magnetism and Magnetic Materials*, 1986, **54**, 1005-1006.
43. I. S. Hagemann, P. G. Khalifah, A. P. Ramirez and R. J. Cava, *Physical Review B*, 2000, **62**, R771-R774.

44. M. Hmoudah, N. N. Nassar, G. Vitale and A. El-Qanni, *RSC Advances*, 2016, **6**, 64482-64493.
45. S. Zhou, W. G. Zeier, M. C. Kemei, M. T. Sougrati, M. Mecklenburg and B. C. Melot, *Inorganic Chemistry*, 2014, **53**, 12396-12401.
46. A. Hethnawi, N. N. Nassar, A. D. Manasrah and G. Vitale, *Chemical Engineering Journal*, 2017, **320**, 389-404.
47. J. Zhao, Y. Zhang, T. Wang, P. Li, C. Wei and H. Pang, *Advanced Materials Interfaces*, 2015, **2**, 1400377-n/a.
48. J. Zhao, M. Zheng, Z. Run, J. Xia, M. Sun and H. Pang, *Journal of Power Sources*, 2015, **285**, 385-392.
49. X. Shi, M. Li, H. Yang, S. Chen, L. Yuan, K. Zhang and J. Sun, *Materials Research Bulletin*, 2007, **42**, 1649-1656.
50. U. Nitsan and T. J. Shankland, *Geophysical Journal International*, 1976, **45**, 59-87.
51. R. Massart, *IEEE Transactions on Magnetics*, 1981, **17**, 1247-1248.
52. M. Pourbaix, *Atlas of Electrochemical Equilibria in Aqueous Solutions*, National Association of Corrosion Engineers, Houston, TX, 2nd edn., 1974.
53. P. J. Chupas, X. Qiu, J. C. Hanson, P. L. Lee, C. P. Grey and S. J. L. Billinge, *Journal of Applied Crystallography*, 2003, **36**, 1342-1347.
54. A. P. Hammersley, S. O. Svenson, M. Han and D. Hauserman, *High Pressure Research*, 1996, **14**, 235-248.
55. P. Juhas, T. Davis, C. L. Farrow and S. J. L. Billinge, *Journal of Applied Crystallography*, 2013, **46**, 560-566.
56. X. J. Yang, P.; Farrow, C. L.; Billinge, S. J. L., 2014.
57. T. Egami and S. J. L. Billinge, *Underneath the Bragg peaks: structural analysis of complex materials*, Elsevier, Amsterdam, 2nd. edn., 2012.
58. C. L. Farrow, P. Juhas, J. W. Liu, D. Bryndin, E. S. Božin, J. Bloch, P. Th and S. J. L. Billinge, *Journal of Physics: Condensed Matter*, 2007, **19**, 335219.
59. C. L. Farrow and S. J. L. Billinge, *Acta Crystallographica*, 2009, **65**, 232.
60. S. Chen, Z. Wei, L. Guo, W. Ding, L. Dong, P. Shen, X. Qi and L. Li, *Chemical Communications*, 2011, **47**, 10984-10986.
61. T. Yamashita and P. Hayes, *Appl Surf Sci*, 2008, **254**, 2441-2449.
62. R. D. Desautels, M. P. Rowe, M. Jones, A. Whallen and J. van Lierop, *Langmuir : the ACS journal of surfaces and colloids*, 2015, **31**, 2879-2884.
63. P. S. Guo and C. X. Wang, *RSC Advances*, 2015, **5**, 70661-70667.
64. R. D. Desautels, J. W. Freeland, M. P. Rowe and J. van Lierop, *Journal of Applied Physics*, 2015, **117**.
65. M. A. Garcia, J. M. Merino, E. Fernandez Pinel, A. Quesada, J. de la Venta, M. L. Ruiz Gonzalez, G. R. Castro, P. Crespo, J. Llopis, J. M. Gonzalez-Calbet and A. Hernando, *Nano Lett*, 2007, **7**, 1489-1494.
66. P. Crespo, P. de la Presa, P. Marin, M. Multigner, J. M. Alonso, G. Rivero, F. Yndurain, J. M. Gonzalez-Calbet and A. Hernando, *Journal of Physics: Condensed Matter*, 2013, **25**, 484006.
67. G. C. Papaefthymiou, *Nano Today*, 2009, **4**, 438-447.
68. T. Tago, T. Hatsuta, K. Miyajima, M. Kishida, S. Tashiro and K. Wakabayashi, *Journal of American Ceramics Society*, 2002, **85**, 2188-2194.

69. A. Casu, M. F. Casula, A. Corrias, A. Falqui, D. Loche and S. Marras, *The Journal of Physical Chemistry C*, 2007, **111**, 916-922.
70. A. L. Tiano, G. C. Papaefthymiou, C. S. Lewis, J. Han, C. Zhang, Q. Li, C. Shi, A. M. M. Abeykoon, S. J. L. Billinge, E. Stach, J. Thomas, K. Guerrero, P. Munayco, J. Munayco, R. B. Scorzelli, P. Burnham, A. J. Viescas and S. S. Wong, *Chemistry of Materials*, 2015, **27**, 3572-3592.
71. M. W. Terban, R. Dabbous, A. D. Debellis, E. Pöselt and S. J. L. Billinge, *Macromolecules*, 2016, **49**, 7350-7358.
72. T. Dykhne, R. Taylor, A. Florence and S. J. Billinge, *Pharmaceutical research*, 2011, **28**, 1041-1048.
73. P. Juhas, C. L. Farrow, X. Yang, K. R. Knox and S. J. Billinge, *Acta Crystallogr A Found Adv*, 2015, **71**, 562-568.
74. C. Manjunatha, B. M. Nagabhushana, H. Nagabhushana and R. P. S. Chakradhar, *J Mater Chem*, 2012, **22**, 22392-22397.
75. Z. Ding, W. Wang, S. Wu and J. P. Liu, *IEEE Transactions on Magnetics*, 2015, **51**, 1-4.
76. H. Hamad, M. Abd El-latif, A. Kashyout, W. Sadik and M. Feteha, *Russian Journal of General Chemistry*, 2014, **84**, 2031-2036.
77. K.-H. Lee, Y.-J. Bae and S.-H. Byeon, in *Nanowires Science and Technology*, ed. N. Lupu, InTech, Rijeka, 2010, DOI: 10.5772/39489, p. Ch. 16.
78. X. Wang and Y. Li, *Angewandte Chemie International Edition*, 2002, **41**, 4790-4793.
79. K. Sue, M. Aoki, T. Sato, D. Nishio-Hamane, S.-i. Kawasaki, Y. Hakuta, Y. Takebayashi, S. Yoda, T. Furuya, T. Sato and T. Hiaki, *Industrial & Engineering Chemistry Research*, 2011, **50**, 9625-9631.
80. E. J. H. Lee, C. Ribeiro, E. Longo and E. R. Leite, *Journal of Physical Chemistry B*, 2005, **109**, 20842-20846.
81. A. Meyer, J. Horbach, W. Kob, F. Kargl and H. Schober, *Physical Review Letters*, 2004, **93**, 027801.
82. B. Miao, W. Zeng, S. Hussain, Q. Mei, S. Xu, H. Zhang, Y. Li and T. Li, *Materials Letters*, 2015, **147**, 12-15.
83. Z.-x. Yang, W. Zhong, Y.-x. Yin, X. Du, Y. Deng, C. Au and Y.-w. Du, *Nanoscale Research Letters*, 2010, **5**, 961-965.
84. L. Hou, H. Hua, S. Liu, G. Pang and C. Yuan, *New Journal of Chemistry*, 2015, **39**, 5507-5512.
85. L. Liu, H. Z. Kou, W. Mo, H. Liu and Y. Wang, *Journal of Physical Chemistry B*, 2006, **110**, 15218-15223.
86. D. Qin, J. Zhou, C. Luo, Y. Liu, L. Han and Y. Cao, *Nanotechnology*, 2006, **17**, 674-679.
87. C. Bao, M. Jin, R. Lu, P. Xue, Q. Zhang, D. Wang and Y. Zhao, *Journal of Solid State Chemistry*, 2003, **175**, 322-327.
88. R. Liu, Y. Jiang, H. Fan, Q. Lu, W. Du and F. Gao, *Chemistry*, 2012, **18**, 8957-8963.
89. C. Z. Wen, H. B. Jiang, S. Z. Qiao, H. G. Yang and G. Q. Lu, *J Mater Chem*, 2011, **21**, 7052.

90. X. Han, M. Jin, S. Xie, Q. Kuang, Z. Jiang, Y. Jiang, Z. Xie and L. Zheng, *Angwandte Chemie International Edition*, 2009, **48**, 9180-9183.
91. Q. Zhang, L. Han, H. Jing, D. A. Blom, Y. Lin, H. L. Xin and H. Wang, *ACS Nano*, 2016, **10**, 2960-2974.
92. M. Mohapatra, D. Behera, S. Layek, S. Anand, H. C. Verma and B. K. Mishra, *Crystal Growth & Design*, 2012, **12**, 18-28.